Asian Journal of Pharmaceutical Sciences 21 (2026) 101123

Available online at www.sciencedirect.com

ScienceDirect

journal homepage: www.elsevier.com/locate/AJPS



Research Article

High-dose treatment of cathepsin B-activatable doxorubicin prodrug nanoparticles that induce tumor-specific immunogenic cell death for immunotherapy of melanoma with minimal systemic toxicity

Yoojeong Oh[a,#], *Jinseong Kim*[a,#], *Nayeon Shim*[a], *Hyeonji Yoo*[a], *Hoyeon Lee*[a,b], *Yumin Jeong*[a,b], *Jagyeong Goo*[c], *Jeongyeon Lee*[a,b], *Mihee Jo*[d], *Hanhee Cho*[a,d,*], *Kwangmeyung Kim*[a,b,*]

[a] *College of Pharmacy, Graduate School of Pharmaceutical Sciences, Ewha Womans University, Seoul 03760, Republic of Korea*
[b] *Graduate Program in Innovative Biomaterials Convergence, Ewha Womans University, Seoul 03760, Republic of Korea*
[c] *Department of Chemical and Biomolecular Enginering, Yonsei University, Seoul 03722, Republic of Korea*
[d] *Research Institute, Noxpharm Co., Ltd., Seoul 03759, Republic of Korea*

ARTICLE INFO

Article history:
Received 7 September 2025
Revised 20 November 2025
Accepted 1 December 2025
Available online 13 January 2026

Keywords:
Cathepsin B-activatable prodrug
Doxorubicin
Melanoma
Immunogenic cell death
Immune checkpoint blockade
Chemo-immunotherapy

ABSTRACT

Highly potent chemotherapy provides rapid therapeutic efficacy in melanoma, but is often limited by drug resistance, off-target toxicity, and systemic toxicity. Combination therapy with chemotherapy and immunotherapy has attracted much attention but still faces challenges such as inconsistent immune responses and systemic toxicity. To address these limitations, we developed cathepsin B-activatable doxorubicin (DOX) prodrug nanoparticles (CatB-NPs) for inducing tumor-specific immunogenic cell death (ICD), while minimizing off-target toxicity in normal tissues with low cathepsin B expression. The cathepsin B-activatable DOX prodrug was synthesized by conjugating the cathepsin B-cleavable peptide (FRRL) to DOX, yielding FRRL-DOX. The amphiphilic FRRL-DOX formed stable nanoparticles (163.6 ± 13.5 nm) through intermolecular hydrophobic interaction and π-π stacking. In melanoma cells overexpressing cathepsin B, CatB-NPs effectively induced cancer cell-specific ICD, while sparing normal cells and immune cells. When CatB-NPs-treated B16F10 cells were co-cultured with immune cells, CatB-NPs enhanced the phagocytic activity of macrophages and induced the maturation of dendritic cells (DCs). In melanoma models, CatB-NPs passively accumulated at tumor tissues through the enhanced permeability and retention effect and were selectively activated by intratumoral cathepsin B, enabling high-dose treatment that induced robust ICD. Importantly, combination therapy with CatB-NPs

* Corresponding authors.
E-mail addresses: ricky1990@snu.ac.kr (H. Cho), kimkm@ewha.ac.kr (K. Kim).
# These authors contributed equally to this work.
Peer review under responsibility of Shenyang Pharmaceutical University.

https://doi.org/10.1016/j.ajps.2026.101123
1818-0876/© 2026 Shenyang Pharmaceutical University. Published by Elsevier B.V. This is an open access article under the CC BY-NC-ND license (http://creativecommons.org/licenses/by-nc-nd/4.0/)

and anti-PD-L1 antibody enhanced ICD, DC maturation and T-cell activation, resulting in complete tumor regression in 50% of treated mice by converting the immunosuppressive tumor environment into an immune-responsive state. In a lung metastasis model, high-dose CatB-NPs with anti-PD-L1 also suppressed metastatic burden without systemic toxicity, supporting their potential as a safe and effective chemo-immunotherapy for melanoma.

© 2026 Shenyang Pharmaceutical University. Published by Elsevier B.V.
This is an open access article under the CC BY-NC-ND license
(http://creativecommons.org/licenses/by-nc-nd/4.0/)

1. Introduction

Melanoma is a highly invasive and metastatic skin cancer, which is a major part of skin-cancer-related deaths [1]. Early melanoma is treated with surgical resection, but if it progresses, chemotherapy, radiotherapy or targeted therapy is required. However, due to its low permeability, high retention rate, and high resistance to conventional treatments, new therapeutics are urgently needed [2,3]. To address these issues, immune checkpoint blockade (ICB) therapies such as anti-CTLA-4 (ipilimumab) and anti-PD-1 (nivolumab) have been approved as the first immunotherapies for melanoma [4]. Interestingly, the combination therapy with ipilimumab and nivolumab extended the 5-year survival rate beyond 50%, with some patients achieving complete remission [5]. However, these responses are limited to some melanoma patients due to the nature of the immunologically cold tumor microenvironment (TME). These cold tumors of melanoma are often characterized by poor T cell infiltration, which is driven by low antigen presentation, insufficient chemokine expression, and inadequate chemokine expression, and highly immunosuppressive TME [6].

To improve ICB responsiveness in melanoma, chemotherapeutic agents that can induce immunogenic cell death (ICD) have emerged as a promising combination therapy [7]. It has been shown that chemotherapeutic agents such as doxorubicin (DOX), oxaliplatin and mitoxantrone trigger ICD by promoting the release of damage-associated molecular patterns (DAMPs), including adenosine triphosphate (ATP, 'find-me' signal), calreticulin (surface-exposed 'eat-me' signal) and HMGB1, respectively. These immunostimulatory DAMPs promote dendritic cell (DC) recruitment, maturation, and antigen uptake, ultimately leading to tumor-specific T cell priming and antitumor immunity [8]. Importantly, early clinical evidence showed that combination therapy with ICD-inducing chemotherapy combined with ICB significantly improved the therapeutic efficacy of malignant melanoma. For example, in a phase I/II trial, DOX combined with pembrolizumab (anti-PD-1 antibody) demonstrated durable disease control in patients with advanced soft tissue sarcoma [9]. This enhanced therapeutic efficacy is attributed to DOX-induced ICD, which promotes DAMPs release, drives DC activation, and enhances tumor-specific T cell priming, thereby complementing PD-1 blockade.

However, melanoma is poorly responsive to standard-dose chemotherapy due to intrinsic drug resistance mechanisms, such as ABCB1 (P-glycoprotein)-mediated drug efflux and phenotypic plasticity characterized by low microphthalmia-associated transcription factor (MITF) and high AXL receptor tyrosine kinase (AXL) expression, which are frequently observed in invasive and drug-resistant melanoma [10]. Furthermore, physical barriers within the TME hinder drug accumulation in tumor tissues, preventing the achievement of concentrations required for robust ICD induction [11]. Given these limitations, high-dose chemotherapy has been explored to enhance intratumoral drug delivery and reach poorly perfused or hypoxic tumor regions [12,13]. High-dose treatment of DOX elevated intratumoral concentrations, resulting in excessive reactive oxygen species (ROS) generation and intensified endoplasmic reticulum (ER) stress, which together increased the frequency and amplitude of DAMPs release [14,15]. Then, the released DAMPs spread within the hypoxic and poorly perfused TME, thereby amplifying the overall antitumor immune response. However, the clinical application of high-dose DOX is limited by severe systemic toxicities. For example, high-dose cisplatin or dacarbazine is restricted by nephrotoxicity and myelosuppression, likewise, high-dose DOX is constrained by cumulative cardiotoxicity, precluding repeated administration [16,17]. Furthermore, high-dose DOX causes immune toxicity by suppressing immune cell function, such as DCs and T cells, leading to systemic immunosuppression. High-dose DOX also triggers systemic inflammation that decreases cytokine levels and impairs macrophage function in chemo-immunotherapy [18]. Therefore, this immunosuppression and inflammation caused by high-dose DOX clearly limited the clinical effectiveness in combination therapy with immune checkpoint inhibitors [19].

Herein, we present cathepsin B-activatable DOX prodrug nanoparticles (CatB-NPs) that enables repeated high-dose administration by minimizing off-target toxicity, while selectively inducing tumor-specific ICD for cancer immunotherapy [20,21]. This tumor-specific ICD induction by CatB-NPs induction not only preserves immune cell viability but also synergizes with anti-PD-L1 antibody (aPD-L1), converting 'immune-cold tumor' into 'immune-hot tumor' to achieve durable tumor regression without systemic toxicity. Previously, we developed the cathepsin B-activatable prodrug by conjugating DOX to a cathepsin B-cleavable peptide (FRRG or FRRL), resulting in amphiphilic FRRG-DOX or FRRL-DOX. Interestingly, the prodrugs formed stable nanoparticles through intermolecular hydrophobic interaction and π-π stacking [22,23]. Then, prodrug nanoparticles were selectively cleaved by cancer cell-overexpressed cathepsin B and the cytotoxic DOX molecules were released from nanoparticles

mainly in cancer cells and tumor tissues, resulting in potent anticancer activity and reduced systemic toxicity in many preclinical models [24,25].

In the present study, the therapeutic potential of combination therapy with CatB-NPs and aPD-L1 was investigated in the B16F10 melanoma model, which represents an 'immune-cold tumor' with poor immune infiltration and limited ICB responsiveness. This strategy overcomes the clinical limitation of not being able to induce effective ICD in melanoma using high-dose DOX. Therefore, this study provides the basis for expanding the therapeutic indication of DOX for melanoma cancer immunotherapy by enabling safe induction of high-dose DOX-derived ICD through cathepsin B-activatable DOX prodrug strategy. The cathepsin-B activatable DOX-derived prodrug was prepared by conjugating self-assembling and cathepsin B-cleavable peptide (FRRL: *Phe-Arg-Arg-Leu*) to DOX, resulting in FRRL-DOX, wherein -RR- peptide sequence can be cleaved by cathepsin B. Furthermore, the prodrug spontaneously self-assembled into stable nanoparticles through intermolecular hydrophobic interaction and π-π stacking. (Scheme 1A). In melanoma tumor models, following intravenous injection, high-dose CatB-NPs can effectively accumulate in tumor tissues *via* the nanoparticle-derived enhanced permeability and retention (EPR) effect [26–28]. Upon internalization by cancer cells, the -RR- peptide sequence is cleaved by cathepsin B in melanoma cells, resulting in the effective release of free DOX at targeted tumor tissues. Then, the released DOX induces melanoma-specific ICD that can trigger the release of immunogenic signals (CRT, ATP, HMGB1), followed by promoting DC maturation and robust activation of tumor-specific T cells. (Scheme 1B). Importantly, combination therapy with CatB-NPs and aPD-L1 not only results in complete regression of primary tumors but also prevents recurrence upon tumor rechallenge, owing to the establishment of long-term immunological memory during treatment (Scheme 1C). Finally, combination therapy with high-dose CatB-NPs and aPD-L1 can effectively suppress the metastatic tumor burden without detectable systemic toxicity in normal tissues, whereas CatB-NPs minimize the off-target toxicity and systemic inflammation in cathepsin B-deficient major organs, such as the heart and spleen (Scheme 1D) [29]. In contrast, free DOX causes widespread off-target toxicity due to non-selective distribution. In the heart, it induces excessive ROS generation, leading to cardiomyocyte damage and myocardial fibrosis [30,31] In the spleen, free DOX impairs macrophage function, resulting in reduced organ size, diminished antigen presentation, and suppressed lymphocyte activation [32]. The combinational therapeutic efficacy and safety of high-dose CatB-NPs with aPD-L1 were carefully evaluated *in vitro* B16F10 cell culture system, melanoma tumor models and lung metastasis models *in vivo*. This strategy overcomes the clinical limitation of not being able to induce effective ICD in melanoma using high-dose DOX. Therefore, this study can provide the basis for expanding the therapeutic indication of DOX for melanoma cancer immunotherapy by enabling safe induction of high-dose DOX-derived ICD through cathepsin B-activatable DOX prodrug strategy.

2. Materials and method

2.1. Materials

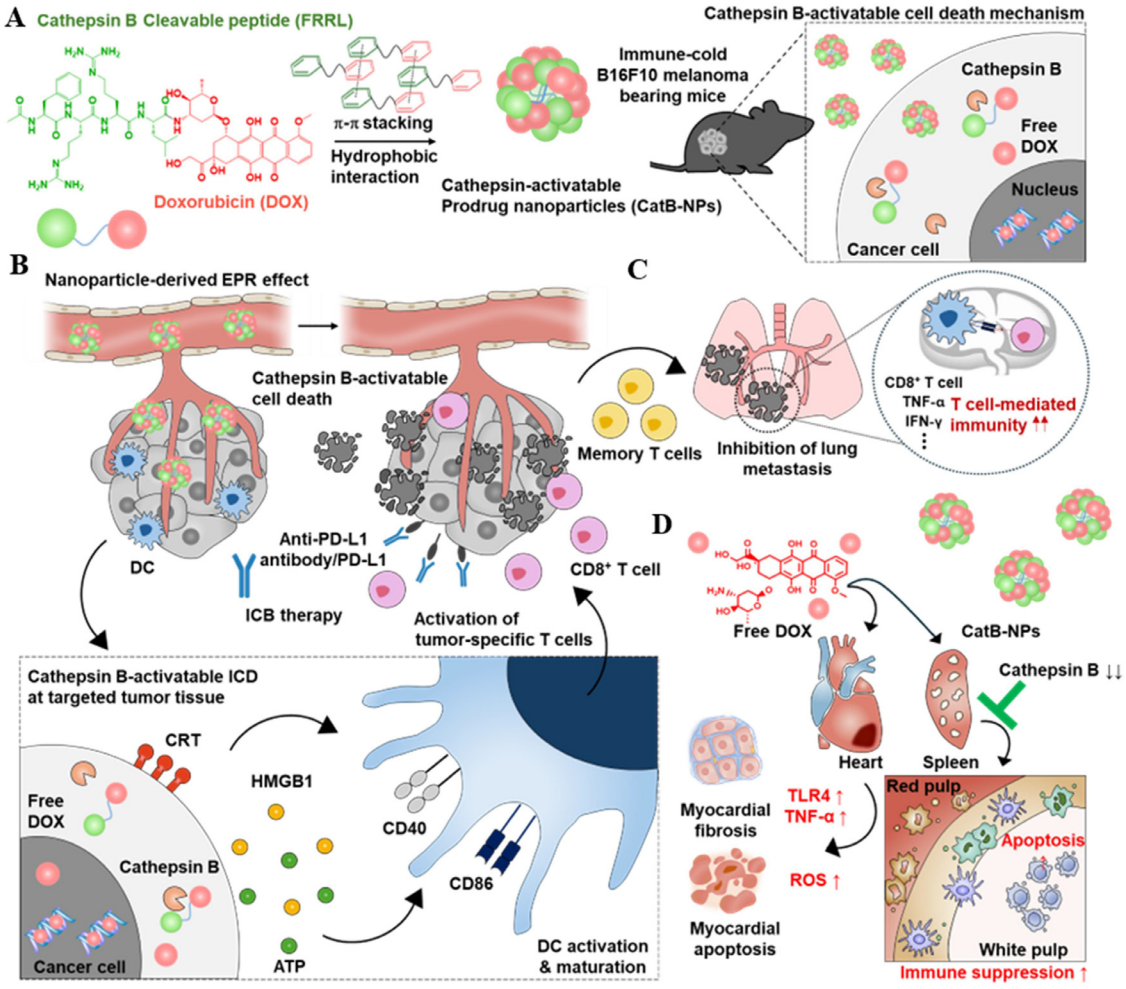
Peptides *Phe-Arg-Arg-Leu* (Ac-FRRL-COOH) and its variants were custom-synthesized by Peptron (Daejeon, Republic of Korea). N-hydroxy succinimide (NHS), 1-ethyl-3-(3-dimethylaminopropyl) carbodiimide (EDC), hematoxylin and eosin (H&E) staining solution, acetonitrile (ACN) and dimethylformamide (DMF) were obtained from Sigma-Aldrich (St. Louis, MO, USA). DOX hydrochloride was supplied by FutureChem (Seoul, Republic of Korea). Recombinant enzymes including cathepsin B, L and S were purchased from R&D Systems (Minneapolis, MN, USA). Monoclonal antibodies against cathepsin B and β-actin, as well as the cathepsin inhibitor benzyloxycarbonyl-Phe-Ala-fluoromethylketone (Z-FA-FMK), were sourced from Santa Cruz Biotechnology (Dallas, TX, USA). Anti-HMGB1 antibody, Alexa Fluor® 647-conjugated anti-calreticulin (CRT) antibody, and the DAB substrate kit were obtained from Abcam (Hanam, Republic of Korea). Cell culture reagents, including RPMI 1640 and DMEM media, fetal bovine serum, and antibiotics (streptomycin and 100 U/ml penicillin), were acquired from Hyclone (USA) and WELGENE Inc. (Daegu, Republic of Korea). The Quanti-Max WST-8 cell viability assay kit was purchased from Biomax (Seoul, Republic of Korea). DCFH-DA was sourced from Sigma-Aldrich (St. Louis, MO, USA). Fluorescent dye-conjugated antibodies specific for mouse CD45, CD3, CD8a, CD4, CD25, F4/80, CD40, CD11c, and CD86were obtained from BioLegend (San Diego, CA, USA). Tumor dissociation kits were sourced from Miltenyi Biotec (Bergisch Gladbach, Germany).

2.2. Synthesis of CatB-NPs

FRRL peptide (790 μmol, 1.0 equiv.) and DOX (1,185 μmol, 1.5 equiv.) were coupled using HATU (948 μmol, 1.2 equiv.) and DIPEA (2,370 μmol, 3.0 equiv.) in anhydrous DMF at room temperature under nitrogen. Briefly, FRRL (790 μmol) was dissolved in dry DMF, followed by the addition of HATU (948 μmol) and DIPEA (2370 μmol). After ~10 min pre-activation (RT, N_2; protected from light), a separate DMF solution of DOX (1,185 μmol) was added dropwise. The reaction mixture was stirred for 6 h at RT under continuous N_2 purging. The crude product was precipitated into cold diethyl ether, collected and purified by semi-preparative reverse-phase HPLC (1260 Infinity II LC system, Agilent Technologies, Santa Clara, CA, USA) using a C_{18} column (150 mm × 20 mm; YMC, Dinslaken, Germany). The identity and purity of the isolated CatB-NPs prodrug were confirmed by ^{1}HNMR (AVANCE NEO Nanobay 400 MHz NMR Spectrometer, Bruker Switzerland AG, Fällanden, Switzerland), equipped at Ewha Drug Development Research Core Center.

2.3. Characterizations of CatB-NPs

The lyophilized prodrug powder was dissolved in distilled water or saline at 1.0 mg/ml to generate nanoparticle suspensions. Uniform dispersion was achieved by probe



Scheme 1 – CatB-activatable DOX nanoparticles (CatB-NPs) inducing ICD to potentiate chemo-immunotherapy with minimal toxicity in melanoma. (A) Cathepsin B-activatable prodrug of FRRL-DOX, constructed with the cathepsin B-cleavable peptide FRRL (Phe-Arg-Arg-Leu) and DOX, is self-assembled into nanoparticles, resulting in CatB-NPs that induce tumor-specific apoptosis in melanoma; (B) In melanoma-bearing mice, CatB-NPs circulate stably and preferentially accumulate in tumor tissues *via* the EPR effect. Within cancer cells, overexpressed cathepsin B cleaves FRRL-DOX into FRRL-P and DOX, triggering tumor-specific ICD accompanied by DAMP signals (CRT, ATP, HMGB1) and promoting DC maturation; (C) ICD-driven immune activation enhances T-cell-mediated immunity, including memory T-cell responses, which eradicate primary tumors and prevent metastatic progression such as lung metastasis; (D) In normal tissues with low cathepsin B, CatB-NPs stay inactive, thereby avoiding cardiac and splenic toxicity and protecting immune cells, while free DOX induces marked cardiotoxicity and systemic immunosuppression.

sonication for 20 s. Stability in saline was monitored at 3, 6, 24 and 48 h by dynamic light scattering (DLS; Zetasizer Nano ZS, Malvern Instruments, Worcestershire, UK), and serum stability was assessed under the same conditions. Morphological features were visualized by transmission electron microscopy (TEM; Tecnai F20 G2, FEI, Hillsboro, OR, USA) following adsorption onto a copper grid, drying and negative staining with 2% uranyl acetate for 1.5 min. For enzymatic degradation assays, the prodrug (1 mg/ml) was incubated in MES buffer (25 mM, pH 5.5) containing cathepsin B (10 μg). Specificity was verified by introducing a cathepsin B inhibitor or comparing cleavage profiles with cathepsin S.

2.4. *In vitro evaluation of cancer cell-specific cytotoxicity of CatB-NPs*

Murine melanoma B16F10 cells and rat cardiomyocyte H9C2 cells were obtained from the Korean Cell Line Bank and maintained in RPMI-1640 medium supplemented with 10% (v/v) fetal bovine serum (FBS; HyClone), 1% streptomycin, and 100 U/ml penicillin at 37 °C in a humidified atmosphere containing 5% CO_2.

The expression of cathepsin B in B16F10 and H9C2 cells was analyzed by western blotting. Briefly, 1×10^6 cells per 100 mm dish were cultured for 24 h, rinsed with PBS, and lysed in ice-cold buffer containing 1% protease inhibitor.

Lysates were centrifuged at 12,000 rpm for 15 min, and protein concentrations in the supernatants were determined using a bicinchoninic acid (BCA) protein assay kit. Equal amounts of protein were resolved on 10% sodium dodecyl sulfate-polyacrylamide gels (SDS-PAGE) and transferred to nitrocellulose membranes. Membranes were blocked in Tris-buffered saline containing 0.1% Tween 20 (TBS-T) and 5% bovine serum albumin (BSA) for 1 h, then incubated with a goat anti-mouse cathepsin B primary antibody (1:1000) at 4 °C for 24 h. After three washes with TBS-T, membranes were incubated with horseradish peroxidase (HRP)-conjugated mouse anti-goat IgG secondary antibody for 1 h. Protein bands were visualized using an enhanced chemiluminescence (ECL) detection system and imaged with an iBright™ CL750 western blot reader (Thermo Fisher Scientific, USA).

For intracellular uptake studies, B16F10 and H9C2 cells were seeded at 2×10^5 cells per 35 mm glass-bottom dish and incubated overnight. Cells were then exposed to either free DOX or CatB-NPs (equivalent to 1 μM DOX) for 24 h at 37 °C. Following treatment, cells were washed twice with phosphate-buffered saline (PBS), fixed in 4% paraformaldehyde for 15 min, and stained with 4′,6-diamidino-2-phenylindole (DAPI) for 13 min in the dark. The subcellular distribution of DOX and CatB-NPs was visualized by confocal laser scanning microscopy (CLSM; Zeiss LSM880 Airyscan, Carl Zeiss AG, Germany, NFEC-2016-05-209580, equipped at Ewha Fluorescence Core Imaging Center), and fluorescence intensities were quantified using Image-Pro software (Media Cybernetics, USA).

Cytotoxicity assays were conducted by seeding B16F10 and H9C2 cells into 96-well plates, followed by a 24 h pre-incubation. Cells were then treated with escalating concentrations of free DOX or CatB-NPs (0–100 μM) and cultured for an additional 24 h. Cell viability was determined using the Cell Counting Kit-8 (CCK-8) assay by adding 20 μl of CCK-8 solution to each well, incubating for 30 min, and measuring absorbance at 450 nm with a microplate reader (Infinite M Nano, Tecan, Switzerland). For intracellular ROS detection, B16F10 cells were seeded at a density of 2×10^5 cells per well in a 24-well plate and incubated for 24 h. The cells were then treated with free DOX or CatB-NPs (2 μM DOX equiv.) for 12 h. After treatment, the cells were washed twice with PBS and incubated with 10 μM DCFH-DA in culture medium for 30 min at 37 °C in the dark. Following gentle washing, the intracellular ROS levels were visualized by monitoring green fluorescence under a fluorescence microscope (EVOS M7000, Thermo Fisher Scientific, USA) equipped with FITC filters.

2.5. DAMPs analysis

To examine the induction of DAMPs by the ICD effect of CatB-NPs and DOX, B16F10 melanoma cells and H9C2 cardiomyocytes were seeded into 35 mm glass-bottom dishes at a density of 1×10^5 cells per dish and allowed to adhere for 24 h. Cells were then exposed to CatB-NPs or free DOX (equivalent to 2 μM DOX) for an additional 24 h. Following treatment, cells were incubated with an Alexa Fluor® 647-CRT antibody at 4 °C for 24 h. After staining, cells were rinsed twice with Dulbecco's PBS (DPBS), fixed with 4% paraformaldehyde for 15 min, and counterstained with DAPI for 15 min. Surface CRT expression was visualized by CLSM and quantified by flow cytometry (CytoFLEX, Beckman Coulter, USA).

2.6. Co-culture assays

Bone marrow-derived macrophages (BMDMs) and dendritic cells (BMDCs) were generated from bone marrow cells isolated from 6-week-old male C57BL/6 mice. For BMDM differentiation, bone marrow cells were cultured with macrophage colony-stimulating factor (M-CSF, 20 ng/ml) for 7 d, with cytokines replenished on Day 1, 2, 3, 4 and 6, and half of the culture medium replaced on Day 4 and 6. BMDCs were obtained by culturing bone marrow cells for 8 d in the presence of interleukin-4 (IL-4, 20 ng/ml), granulocyte- M-CSF (GM-CSF, 20 ng/ml), and 0.1% β-mercaptoethanol.

To assess the release of other ICD-associated signals, the culture supernatant of B16F10 cells treated with CatB-NPs or DOX was collected for high mobility group box 1 (HMGB1) and ATP measurements. HMGB1 levels were determined *via* western blotting, while ATP secretion was quantified using an ATP assay kit. The phagocytic uptake of tumor cells by BMDMs was evaluated using B16F10 cells pretreated with CatB-NPs or DOX (2 μM DOX equi.) for 24 h. Prior to co-culture, BMDMs were labeled with CellTracker™ Green for 30 min at room temperature, washed with DPBS, and resuspended in complete culture medium. Separately, B16F10 cells were harvested, washed with PBS, adjusted to 1×10^7 cells in 50 mL PBS, and stained with pHrodo™ Deep Red (120 ng/ml) for 30 min under gentle agitation. Labeled tumor cells were washed, resuspended in fresh medium, and co-incubated with BMDMs for 2 h. Non-adherent cells were removed by gentle DPBS washing, and phagocytosis was imaged by CLSM. To investigate DC maturation triggered by ICD, B16F10 cells (1×10^6 cells) were seeded into 100 mm culture dishes and treated with CatB-NPs or DOX (2 μM DOX equiv.) for 24 h. After treatment, tumor cells were co-cultured with BMDCs for 24 h. The proportion of mature DCs ($CD11c^+CD40^+CD86^+$) within the co-culture was quantified by flow cytometry.

2.7. In vivo tumor-targeting behavior of CatB-NPs in B16F10-bearing mice

6-week-old male C57BL/6 mice (Nara Bio, Korea) were maintained under specific pathogen-free conditions, and all animal procedures followed the IACUC guidelines of Ewha Womans University (Approval No. 22-073-7). To evaluate the systemic pharmacokinetics of CatB-NPs, C57BL/6 mice received an intravenous injection of free DOX or CatB-NPs at DOX-equivalent doses of 5 mg/kg (L) or 10 mg/kg (H). Blood samples were collected at 20 and 40 min, and at 1, 3, 6, 24 and 48 h post-injection, centrifuged at 4500 × *g* to obtain plasma, and analyzed by HPLC to determine plasma DOX concentrations and calculate $T_{1/2}$, C_{max} and AUC. For biodistribution studies, B16F10 tumors were established by

subcutaneous inoculation of 1×10^6 B16F10 cells into the left thigh of C57BL/6 mice ($n = 3$). When tumors reached ~200 mm^3, mice were intravenously administered free DOX or CatB-NPs at 5 mg/kg (L) or 10 mg/kg (H) DOX equivalent. Because melanotic B16F10 tumors severely attenuate optical signals, whole-body NIRF imaging was not performed. Instead, biodistribution was evaluated by direct tissue quantification. At 24 h post-injection, tumors and major organs (liver, lung, spleen, kidney and heart) were collected, rinsed, homogenized, and analyzed for DOX-associated fluorescence using an IVIS Lumina Series III system. To examine cathepsin B-mediated activation of FRRL-DOX *in vivo*, tumors collected at 24 h post-injection were homogenized and extracted for LC-MS analysis. Samples were analyzed to detect L-DOX (the cathepsin B-derived cleavage product) and DOX generated through metabolic conversion of L-DOX. Saline-treated tumor tissues served as negative controls.

2.8. *In vivo antitumor efficacy and immune response of CatB-NPs in melanoma-bearing mice*

Mice bearing subcutaneous B16F10 tumors (50 ± 13 mm^3) were randomized into four treatment groups: saline, free DOX, CatB-NPs (L; 5 mg/kg DOX equiv.), or CatB-NPs (H; 10 mg/kg DOX equiv.). Treatments were administered intravenously every 3 d Tumor dimensions were measured with calipers, and volumes were calculated as longest diameter × (shortest diameter)^2 × 0.53 at 2-d intervals until 12 d Animals with tumor volumes exceeding 2000 mm^3 were removed from the study.

Tumor tissues were fixed in 4% paraformaldehyde, embedded in paraffin, and sectioned at a thickness of 8 μm. For H&E staining, sections were deparaffinized, rehydrated and sequentially stained with H&E staining solution. Apoptotic cells were identified using a terminal deoxynucleotidyl transferase dUTP nick-end labeling (TUNEL) assay kit following the manufacturer's instructions, followed by DAPI counterstaining. All stained sections were visualized using a fluorescence microscope.

To evaluate DAMP expression associated with the ICD effects of CatB-NPs and DOX, single-cell suspensions were prepared from excised tumor tissues and stained with an Alexa Fluor® 647-CRT antibody at 4 °C for 24 h. After washing twice with DPBS, the stained cells were analyzed by flow cytometry. HMGB1 and ATP released from tumor homogenates were quantified by Western blot analysis and an ATP assay kit, respectively.

Antitumor immune responses were assessed on Day 12 post-treatment by collecting tumors, spleens, lymph nodes and blood samples. Tumors were enzymatically dissociated using a Tumor Dissociation Kit, whereas spleens were mechanically processed by gently pressing the tissue through a 0.45 μm strainer. Cell suspensions were incubated with an Fc receptor blocker for 10 min to minimize nonspecific binding, followed by staining with a multi-parameter antibody panel for 1 h at 4 °C.

For immune cell analysis, 100 μl whole blood was collected into heparin- or EDTA-coated tubes, stained with fluorophore-labeled antibodies for 30 min at room temperature in the dark, followed by red blood cell lysis and fixation of leukocytes with 4% paraformaldehyde. Immune cell populations in tumors, spleens and lymph nodes were analyzed by flow cytometry using the antibody panel. After staining, all samples were centrifuged at 450× *g* for 5 min at 4 °C, washed twice with PBS, and resuspended for analysis. For immunohistochemical (IHC) analysis, tumor sections were incubated overnight at 4 °C with antibodies against CD8, CD69, IFN-γ and CD25 to evaluate the activation status of $CD8^+$ T cells.

2.9. *Therapeutic efficacy CatB-NPs combined with APD-L1 in B16F10 tumor-bearing mice*

To evaluate the efficacy of combination therapy and the associated antitumor immune responses, B16F10 tumor-bearing mice were randomly divided into four groups: (1) saline, (2) aPD-L1, (3) DOX (5 mg/kg) + aPD-L1, and (4) CatB-NPs (H) (equivalent to 10 mg/kg DOX) + aPD-L1. DOX or CatB-NPs were administered intravenously every 3 d, and aPD-L1 antibody was given intraperitoneally at the same interval.

On Day 12, tumors, spleens, lymph nodes and blood were harvested for immune response analyses. Tumor sections were subjected to H&E and TUNEL staining to evaluate morphological changes and apoptosis. All groups were further monitored until Day 30 to assess tumor growth and survival following the treatment period.

On Day 42, mice that had achieved complete regression (CR) in the CatB-NPs (H) + aPD-L1 group were intravenously rechallenged with 4×10^5 B16F10 cells. Naïve mice were included as controls. Tumor growth was monitored every 2 d, and on Day 54 (12 d post-rechallenge), spleens were collected for immune memory analyses. Effector/memory $CD8^+$ T cells ($CD3^+CD8^+CD44^+CD62L^{low}$) were quantified by flow cytometry, and the functional activation of memory T cells was further assessed by measuring IFN-γ and TNF-α secretion using ELISA.

2.10. *Therapeutic efficacy of CatB-NP in a B16F10 lung metastasis model*

Lung metastasis model was established by intravenously injecting C57BL/6 mice with luciferase-expressing B16F10 cells (4×10^5 cells in 100 μl PBS). 5 d after tumor inoculation, mice were randomly assigned to five groups: (1) saline, (2) free DOX (5 mg/kg, DOX equiv.), (3) CatB-NPs (H) (10 mg/kg, DOX equiv.), (4) DOX + aPD-L1, and (5) CatB-NPs (H) + aPD-L1. DOX or CatB-NPs were administered intravenously every three d, while the aPD-L1 antibody (10 mg/kg) was given intraperitoneally at the same interval. Tumor progression was monitored at predetermined time points by noninvasive bioluminescence imaging (IVIS Lumina Series III system, PerkinElmer, Waltham, MA, USA).

2.11. *In vivo safety evaluation of CatB-NPs in C57BL/6 mice*

To evaluate the *in vivo* safety of CatB-NPs, C57BL/6 mice were intravenously administered free DOX, CatB-NPs (L; 5 mg/kg DOX equiv.), or CatB-NPs (H; 10 mg/kg DOX

equiv.) every 3 d following the same treatment schedule. Body weight was monitored every 2 d, and animals were considered dead for survival analysis once body weight decreased by 15%−20% of the initial value or when tumor volume exceeded 2000 mm^3, spleen and heart weights were measured at the endpoint. Systemic toxicity was assessed through serum biochemical analyses, including hepatic function markers (alkaline phosphatase [ALP], alanine aminotransferase [ALT], aspartate aminotransferase [AST]), renal function (blood urea nitrogen [BUN]), metabolic activity (triglyceride [TG]), and hematological parameters (mean corpuscular hemoglobin concentration [MCHC], platelet count [PLT], white blood cells [WBC], lymphocytes [LYM], and neutrophils [NEUT]). To evaluate cardiotoxicity and splenic toxicity, harvested tissues were processed and stained according to standard immunohistochemistry protocols. Cardiac tissues were analyzed for apoptosis (TUNEL and H&E staining), fibrosis (Sirius Red staining), and inflammation, whereas splenic tissues were assessed for apoptosis (TUNEL and H&E staining) and inflammation (TLR4 immunostaining).

2.12. *Statistical analysis*

All statistical analyses were performed using GraphPad Prism 8. Data is presented as the mean ± standard deviation (SD) from at least three independent experiments. Comparisons between two groups were analyzed by Student's *t*-test, while comparisons among three or more groups were performed using one-way analysis of variance (ANOVA) followed by Tukey-Kramer post-hoc test. Significance levels are denoted as $^{*}P < 0.05$, $^{**}P < 0.01$, $^{***}P < 0.001$ and $^{****}P < 0.0001$.

3. Result and discussion

3.1. *Physicochemical properties of CatB-NPs*

To engineer a cancer cell-specific DOX prodrug capable of inducing ICD, the cathepsin B-cleavable peptide sequence FRRL (*Phe-Arg-Arg-Leu*) was first synthesized *via* solid-phase peptide synthesis (SPPS). The C-terminal carboxyl group of FRRL was then conjugated to the primary amine group of DOX through amide bond formation using HATU and DIPEA in DMF as coupling agents (Fig. 1A and S1). The crude product was purified by RP-HPLC equipped with a C_{18} column, affording FRRL-DOX with a purity of >95% (Fig. S2). The molecular weight of the purified FRRL-DOX was confirmed by LC-MS (*m/z* 1158.8 $[M + H]^+$), consistent with the calculated value of the expected molecular ion (Fig. 1B), and the chemical structure of FRRL-DOX was further validated by NMR spectroscopy, showing its new amide bond at 8.21 ppm (Fig. S3). From these data, the self-assembling and cathepsin B-cleavable prodrug FRRL-DOX was easily synthesized using a one-step reaction that can enables scalable and cost-effective mass production.

The freshly prepared FRRL-DOX (1 mg/ml) formed stable nanoparticles in saline, yielding CatB-NPs with an average size of 163.6 ± 13.5 nm and a PDI of 0.322 ± 0.195, as determined by DLS, indicating a narrow size distribution. Additionally, CatB-NPs (1 mg/ml) in distilled water showed a uniform spherical morphology in TEM images (Fig. 1C). It has been reported that the intermolecular π-π stacking of benzene rings of both F and DOX in FRRL-DOX greatly influences the self-assembled nanoparticle structure in aqueous conditions. Consistent with this mechanism, it has been reported that nanoparticles formed from small peptides, prodrugs or drug-drug conjugates containing *Phe* residues or aromatic moieties exhibit highly stable nanoparticle structure through π-π stacking in physiological conditions [22,23]. Furthermore, CatB-NPs maintained their nanoparticle structure with minimal size changes for up to 48 h in saline, indicating their substantial stability under physiological conditions (Fig. 1D and S4). Although a slight increase in average size was observed in plasma at 37 °C, CatB-NPs remained well dispersed with a narrow size distribution throughout the 48-h period. These results indicate that CatB-NPs preserve their structural integrity in plasma without detectable dissociation or aggregation. This stability of CatB-NPs suggests that CatB-NPs are suitable for tumor targeting delivery through the EPR effect, enabling effective accumulation in targeted tumor tissues [24,33]. Next, cathepsin B-specific cleavage of CatB-NPs (1 mg/ml) were assayed in the presence of lysosomal enzyme of cathepsin B. When CatB-NPs were incubated with cathepsin B (10 μg/ml) in pH 5.5 MES buffer at 37 °C for 24 h, a new L-DOX peak at 15.4 min appeared in the HPLC spectrum after 3 h of incubation and the L-DOX peak increased to 90% within 9 h, indicating that -RR- sequence of FRRL-DOX was cleaved by cathepsin B (Fig. 1E). The molecular weight of the cleaved L-DOX (679.4 *m/z* $[M+Na]^+$) was also confirmed through LC-MS analysis (Fig. 1F). As a control, no cleavage of CatB-NPs was observed in the presence of cathepsin B inhibitor or cathepsin S, confirming that CatB-NPs remain stable in the absence of cathepsin B under physiological conditions. (Fig. 1G and 1H). Collectively, these findings confirmed that CatB-NPs can be specifically activatable by cathepsin B with high stability and tumor-specific activation.

3.2. *Cancer cell-specific ICD induction of CatB-NPs in melanoma cell cultured system*

Firstly, the cathepsin B-activatable cancer cell death mechanism was investigated in B16F10 melanoma cells, an immune-cold tumor model characterized by poor T cell infiltration [34]. Rat cardiomyocytes (H9C2) with minimal cathepsin B expression served as normal cell controls. As expected, B16F10 cells exhibited 5.3 ± 1.0-fold higher cathepsin B expression than H9C2 cells (Fig. 2A), highlighting the potential of cathepsin B-activatable approaches for selective cancer cell targeting in immune-cold tumors. The cathepsin B-activatable DOX release from CatB-NPs was then evaluated in B16F10 and H9C2 cells using CLSM. After 24 h treatment under a mildly toxic condition that preserved the adherent cell morphology, both free DOX (1 μM) and CatB-NPs (1 μM) predominantly accumulated in the nuclei of B16F10 cells, consistent with the nuclear localization requirements for inhibiting topoisomerase II [35]. In contrast, free DOX exhibited ~89% nuclear localization in H9C2 cells, whereas CatB-NPs showed only ~10%, remaining mainly in the cytoplasm, indicating the cathepsin B-activatable DOX release of CatB-NPs in the nuclear compartment of B16F10 cells.

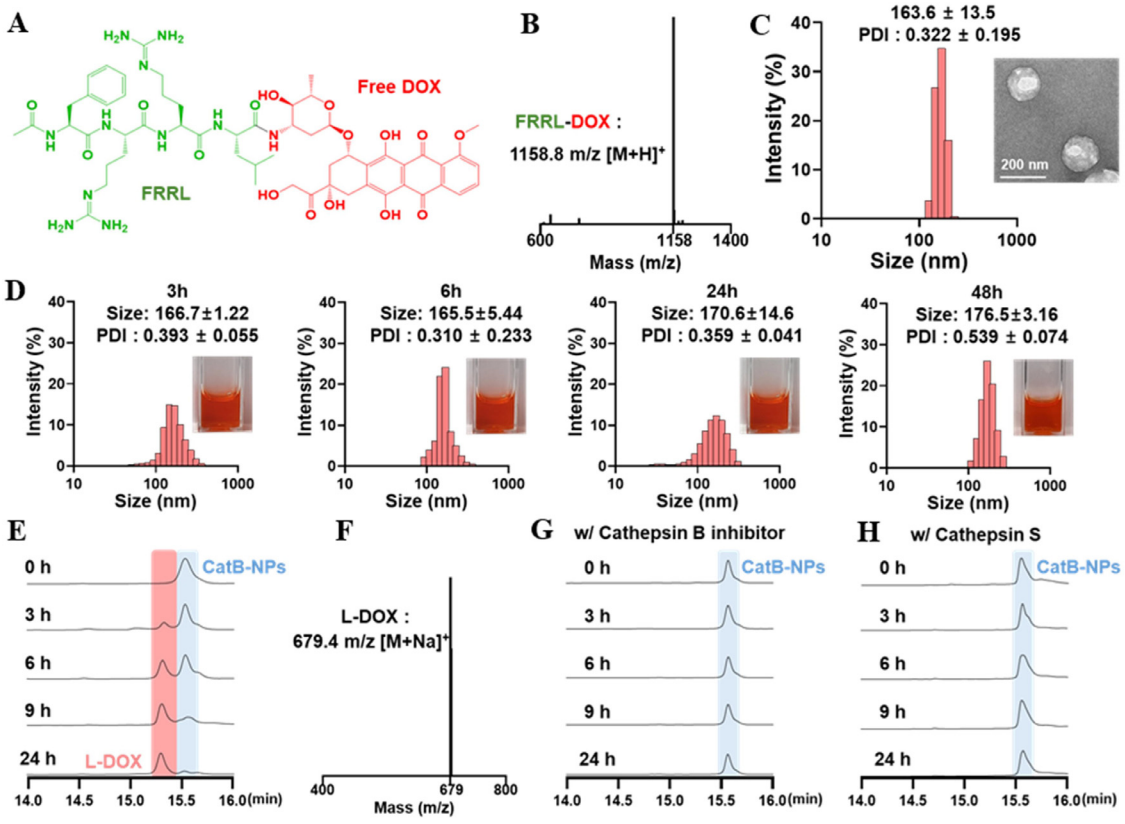


Fig. 1 – Preparation of cathepsin B-cleavable self-assembling prodrug nanoparticles (CatB-NPs). (A) Chemical structure of FRRL-DOX (CatB-NPs) and (B) LC-MS analysis results. (C) Size distribution and PDI of CatB-NPs in saline (1 mg/ml) and TEM image of CatB-NPs in distilled water (1 mg/ml) negatively stained with uranyl acetate. (D) Stability of CatB-NPs in saline (1 mg/ml) for 3, 6, 24 and 48 h. (E) HPLC spectrum of CatB-NPs (1 mg/ml) incubated with cathepsin B (10 μg) in MES buffer (25 mM, pH 5.5) at 37°C for 24 h. (F) MALDI-TOF analysis showing cathepsin B-mediated cleavage of CatB-NPs to release L-DOX, and (G) HPLC spectrum of CatB-NPs incubated with cathepsin B inhibitor or (H) cathepsin S.

To further validate the cathepsin-activatable DOX release mechanism, B16F10 cells were pretreated with the cathepsin B inhibitor (Z-FA-FMK) at 10 μM for 1 h, followed by treatment with CatB-NPs or free DOX at 1 μM. Inhibition of cathepsin B drastically reduced the nuclear localization of CatB-NPs, with over 90% of the fluorescence retained in the cytoplasm, indicating their dependence on cathepsin B-activatable DOX release in melanoma cells. By contrast, free DOX still showed predominant nuclear accumulation of ~90% in cathepsin B inhibitor-treated B16F10 cells (Fig. 2B and S5). Given the cathepsin B-activatable DOX release of CatB-NPs demonstrated by CLSM, we next evaluated their cytotoxic effects in B16F10 and H9C2 cells using the CCK assay. In B16F10 cells, CatB-NPs exhibited a higher IC_{50} of 1.87 μM than free DOX at 0.13 μM, reflecting the additional time required for cathepsin B-mediated prodrug activation [24]. In contrast, CatB-NPs showed notably reduced cytotoxicity in H9C2 cells, with an IC_{50} of 203.1 μM compared to 0.1 μM for free DOX, corresponding to an approximately 108-fold difference between H9C2 and B16F10 (Fig. 2C, 2D and S6).

Next, we evaluated whether CatB-NPs could induce cathepsin B-activatable ICD while minimizing toxicity to normal cells. To establish consistent ICD-inducing conditions in B16F10 cells, we selected DOX-equivalent concentration of 2 μM, which is close to the IC_{50} of CatB-NPs. Because DOX-induced ICD is typically mediated by ROS generation, intracellular ROS levels were first assessed using DCFH-DA staining. As we expect, strong ROS fluorescence was observed in both free DOX- and CatB-NP-treated B16F10 cells, supporting that CatB-NPs successfully induce ROS generation that may promote DAMP release and subsequent induction of ICD (Fig. S7). We then examined CRT expression in B16F10 and H9C2 cells treated with 2 μM free DOX or 2 μM CatB-NPs using CLSM and fluorescence-activated cell sorting (FACS). CLSM analysis revealed strong CRT signals on the surface of B16F10 cells after 24 h treatment with both free DOX and CatB-NPs. In contrast, no CRT induction was observed in H9C2 cells treated with CatB-NPs, whereas free DOX showed minimal CRT induction on the surface of H9C2 cells. FACS analysis confirmed that in B16F10 melanoma cells, both free DOX and CatB-NPs induced similarly strong ICD, with CRT exposure increasing 4.6-fold and 4.7-fold, respectively, compared to the control (Fig. 2D). By contrast, in H9C2 cardiomyocytes, free DOX triggered an 11.9-fold increase in CRT exposure, whereas CatB-NPs induced only a 2.7-fold increase, highlighting that ICD induction by CatB-NPs occurs predominantly in tumor cells (Fig. 2E and S8). These findings highlight that CatB-NPs selectively induce cathepsin B-activatable ICD in cancer

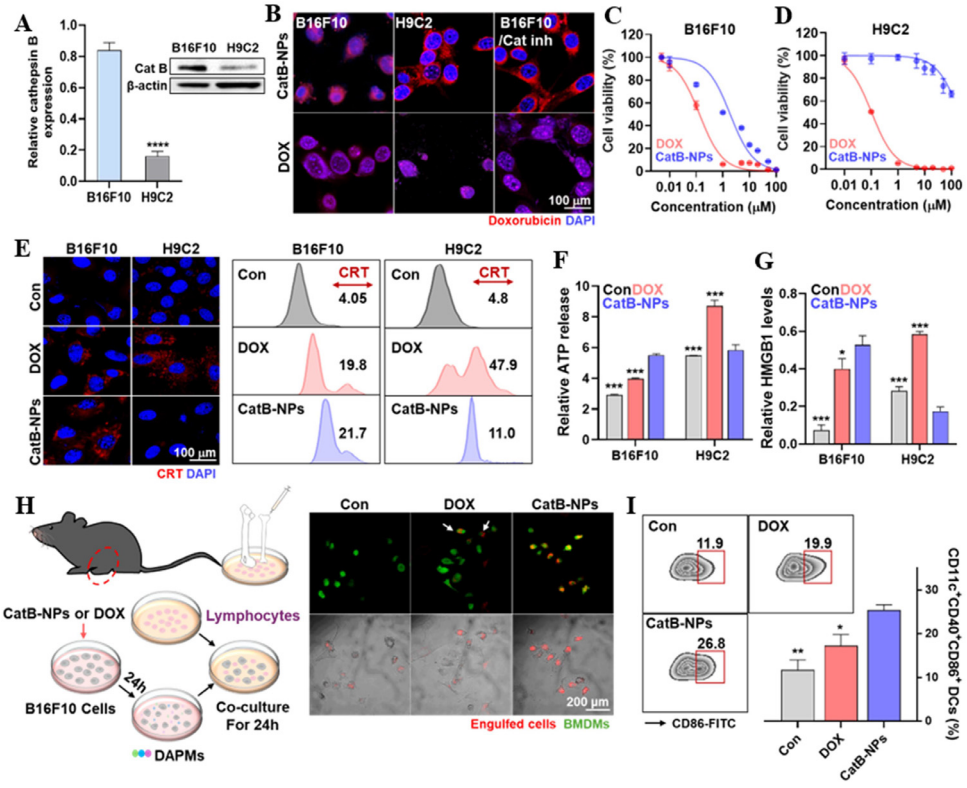


Fig. 2 – Cancer cell-specific activation of CatB-NPs and induction of ICD in immune-cold melanoma cells. (A) Western blot analysis and quantification of cathepsin B expression in B16F10 cancer cells and H9C2 normal cells; (B) Confocal fluorescence images of B16F10 and H9C2 cells treated with free DOX or CatB-NPs (1 μM DOX equivalent) for 24 h, with or without the cathepsin B inhibitor Z-FA-FMK (blue: DAPI, red: DOX); (C, D) Cell viability of B16F10 cancer cells and H9C2 normal cells after 24 h treatment with free DOX or CatB-NPs; (E) Confocal microscopy and flow cytometry analyses of CRT exposure in B16F10 and H9C2 cells after 24 h treatment with PBS, DOX or CatB-NPs (red: CRT, blue: DAPI); (F, G) Quantification of ATP release and HMGB1 secretion in B16F10 and H9C2 cells treated with PBS, DOX or CatB-NPs for 24 h; (H) Confocal images of BMDMs co-cultured with B16F10 cells pretreated with DOX or CatB-NPs (red: B16F10 cells, green: BMDMs); (I) Flow cytometry of mature DCs ($CD11c^+CD40^+CD86^+$) after co-culture with pretreated B16F10 cells.

cells while minimizing toxicity to normal cells. To further evaluate ICD induction, we quantified extracellular ATP and HMGB1 release in cancer and normal cells. In B16F10 cells, ATP release increased 1.36-fold with free DOX and 1.89-fold with CatB-NPs compared with the control group. In contrast, in H9C2 cells, ATP release increased 1.59-fold with free DOX but only 1.05-fold with CatB-NPs, indicating that CatB-NPs selectively trigger ICD in melanoma cells while minimizing chemotherapy-induced toxicity in normal cells (Fig. 2F and 2G).

To assess immune activation triggered by the cathepsin B-activatable ICD of CatB-NPs, B16F10 cells were pretreated for 24 h with either 2 μM free DOX or 2 μM CatB-NPs and labeled with the pH-sensitive dye pHrodo succinimidyl ester (red fluorescence in acidic phagosomes). These cells were then co-cultured for 2 h with BMDMs from C57BL/6 mice labeled with Cell Tracker™ Green [36]. CLSM imaging revealed a notably higher number of engulfed CatB-NPs-treated B16F10 cells (red color) within BMDMs (green color) compared with free DOX (Fig. 2H). This enhanced phagocytic activity of co-cultured macrophages likely arises from the cathepsin B-activatable ICD induced by CatB-NPs, which reduces chemotherapy-induced toxicity in macrophages. Furthermore, to quantify DC maturation, immature BMDCs were co-cultured for 2 h with B16F10 cells pretreated with 2 μM free DOX or 2 μM CatB-NPs. As expected, CatB-NPs increased the proportion of mature DCs ($CD11c^+CD40^+CD86^+$) by ~2.16-fold compared with untreated controls and by ~1.46-fold relative to free DOX (Fig. 2I), consistent with cathepsin B-activatable ICD induction and reduced chemotherapy-associated toxicity. From these results, we assume that cathepsin B-activatable ICD of CatB-NPs preserves immune cell viability and promotes immunostimulatory signaling, providing a more favorable immune environment for chemo-immunotherapy.

3.3. *Antitumor efficacy of CatB-NPs supported by in vivo delivery and activation in B16F10 melanoma*

Before evaluating the antitumor efficacy of CatB-NPs in B16F10 tumors, we first characterized their *in vivo* pharmacokinetics and tumor-localization behavior to verify that the formulation can achieve effective intratumoral delivery. Pharmacokinetic analysis in C57BL/6 mice showed that CatB-NPs markedly prolonged systemic exposure compared with free DOX; CatB-

NPs (L) increased $T_{1/2}$, C_{max} and AUC by 5.42-, 38.25- and 44.37-fold, and CatB-NPs (H) resulted in 4.49-, 83.81-, and 79.22-fold increases, respectively (Fig. S9a). The sustained circulation provided by the stable nanostructure of CatB-NPs suggests enhanced passive tumor targeting through the EPR effect. Because melanotic B16F10 tumors severely attenuate optical signals, biodistribution was assessed by directly quantifying DOX fluorescence in tissue homogenates rather than whole-body NIRF imaging. At 24 h post-injection, free DOX was almost completely cleared from tumors, whereas CatB-NPs (L) and (H) produced 1.46- and 1.84-fold higher intratumoral fluorescence, respectively (Fig. S9b), demonstrating efficient EPR-driven tumor localization. To verify whether the strong intratumoral DOX accumulation originated from cathepsin B-mediated activation, we performed LC-MS analysis. No DOX-related signals were detected in saline-treated tumors, whereas tumors from CatB-NPs (H) displayed clear m/z peaks corresponding to L-DOX, the primary cathepsin B cleavage product, and free DOX generated through subsequent metabolism of L-DOX (Fig. S9c). Major organs showed only physiological fluorescence patterns associated with hepatic metabolism and renal elimination, with no histological abnormalities observed (Fig. S9d and S19-S20). Together, these results verify that CatB-NPs undergo prolonged circulation, passive EPR-mediated tumor accumulation, and intratumoral enzymatic activation, which provides a mechanistic basis for interpreting the subsequent antitumor efficacy.

The dose-dependent antitumor efficacy of CatB-NPs was evaluated in B16F10 melanoma-bearing mice. In the high-dose free DOX group, average body weight loss exceeded 20% by 4–6 d, reaching the ethical endpoint threshold and leading to premature termination of the group, accompanied by a sharp decline in survival (Fig. S10). In contrast, CatB-NPs (H) group maintained a stable body weight despite repeated high-dose administration, enabling safe long-term treatment and survival evaluation. This demonstrates that CatB-NPs (H) can achieve prolonged high-dose treatment with improved safety. When the tumor volumes reached approximately 50 ± 13 mm^3, each formulation was intravenously administered once every 3 d After 12 d of treatment, high-dose CatB-NPs (H) group (132.34 ± 15.41 mm^3) exhibited the most pronounced tumor growth inhibition compared with the saline group (2331.35 ± 145.62 mm^3), free DOX group (767.35 ± 282.47 mm^3), and low-dose CatB-NPs (L) group (389.02 ± 190.97 mm^3), respectively (Fig. 3A). As a control, saline-treated mice were euthanized on Day 12 in accordance with ethical guidelines due to excessive tumor burden (>2000 mm^3). At Day 12, the mean tumor weight of high-dose CatB-NPs (H) group (0.13 ± 0.07 g) was approximately 16.5-fold, 6.2-fold, and 5.8-fold lower than that of the saline-treated group (2.14 ± 0.13 g), free DOX group (0.80 ± 0.03 g), and low-dose CatB-NPs (L) group (0.76 ± 0.03 g), respectively. This superior antitumor efficacy of CatB-NPs (H) can be attributed to their enhanced tumor accumulation through the EPR effect, which enables efficient tumor-specific drug delivery while minimizing off-target toxicity in normal tissues and preserving immune cell functionality [33]. The images of excised tumors confirmed these consistent tumor-suppressive effects with reliable reproducibility (Fig. 3B). Histopathological analysis with H&E staining revealed dose-dependent extensive structural collapse and apoptosis in high-dose CatB-NPs (H) group, significantly exceeding the levels observed in the free DOX and low-dose CatB-NPs (L) groups. Consistently, TUNEL staining further confirmed extensive apoptotic cell death in high-dose CatB-NPs (H) group (Fig. 3C and 3D). Importantly, while low-dose CatB-NPs (L) already showed superior tumor inhibition compared with saline and free DOX groups, the high-dose CatB-NPs (H) group achieved significantly higher efficacy without body weight loss or death during treatment, highlighting the safety of long-term high-dose administration.

To further evaluate cathepsin B-activatable ICD induction by CatB-NPs, antitumor immune responses were analyzed on Day 12 by FACS. The proportion of CRT-positive tumor cells increased by 1.13-fold with free DOX and by 1.56-fold with low-dose CatB-NPs (L), whereas high-dose CatB-NPs (H) achieved the highest induction at 2.56-fold relative to the saline group (Fig. 3E). Consistently, extracellular HMGB1 levels rose by 7.22-fold, 9.53-fold, and 22.41-fold, and ATP release increased by 3.21-fold, 3.10-fold, and 4.21-fold with free DOX, low-dose CatB-NPs (L), and high-dose CatB-NPs (H), respectively (Fig. 3F and 3G). Collectively, these findings indicate that high-dose CatB-NPs, through enhanced intratumoral accumulation, elicit robust ICD by promoting DAMPs release, thereby overcoming intrinsic drug resistance and potentiating antitumor immunity in melanoma. Moreover, repeated high-dose administration of CatB-NPs preserved the viability and functional integrity of immune cells, as evidenced by marked increases in the populations of mature dendritic cells ($CD11c^+CD40^+CD86^+$) and cytotoxic T cells ($CD45^+CD3^+CD8^+$) without any indication of immune cell depletion or systemic immunotoxicity (Fig. 3H and 3I).

Consistently, immunofluorescence staining of tumor tissues revealed the highest infiltration of $CD8^+$ T cells in the high-dose CatB-NPs (H) group, further confirming its superior capacity to elicit antitumor immune responses (Fig. S11). While both low-dose CatB-NPs (L) and high-dose CatB-NPs (H) reduced intratumoral regulatory T cells (Tregs, $CD3^+CD4^+CD25^+$), the high-dose treatment further amplified these immunomodulatory effects, resulting in a more profound conversion of the immunosuppressive TME into an immune-responsive milieu (Fig. 3J and S12). From these results, high-dose CatB-NPs (H) enabled safe and repeated administration and produced clear dose-dependent antitumor activity. The robust induction of tumor-specific ICD by high-dose CatB-NPs (H) provides a strong rationale for subsequent evaluation of their capacity to enhance anti-tumor immunity without systemic toxicity.

3.4. *Synergistic antitumor efficacy of CatB-NPs and APD-L1 with durable immune memory in B16F10 melanoma*

In the previous section, we confirmed that CatB-NPs elicited dose-dependent tumor inhibition and cathepsin B-activatable ICD induction. Therefore, we further evaluated whether high-dose CatB-NPs (H) could enhance the efficacy of ICB when combined with aPD-L1, aiming to achieve more durable therapeutic outcomes and long-term immune protection. This starting volume was selected in consideration of the rapid growth rate of melanoma tumors, allowing sufficient

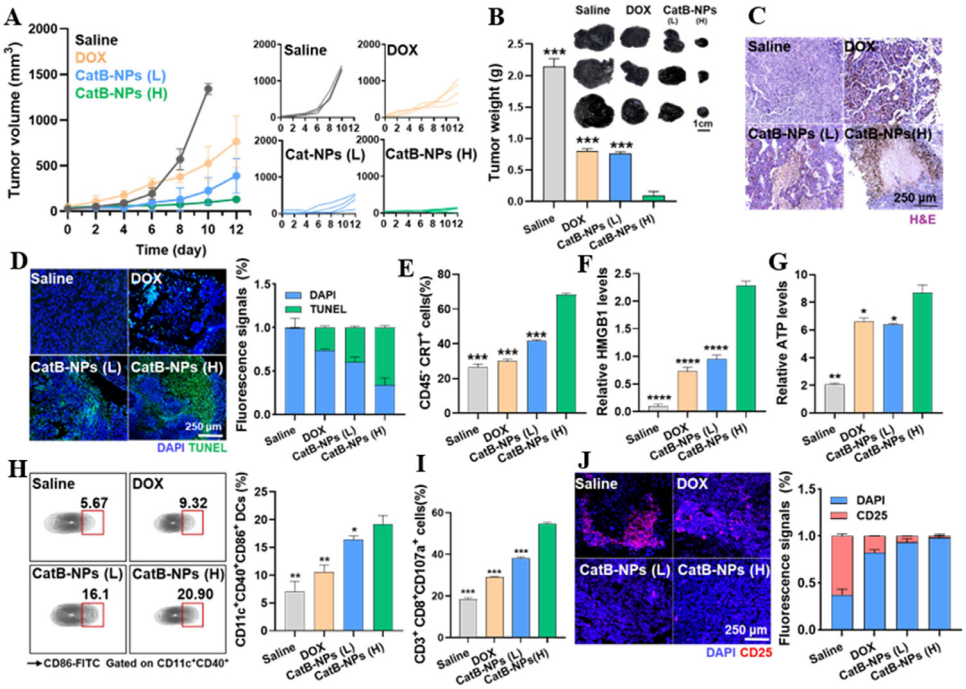


Fig. 3 – Antitumor efficacy and ICD-related immune activation of CatB-NPs in B16F10 melanoma-bearing mice. (A) Tumor growth curves in C57BL/6 mice ($n = 4$) bearing B16F10 melanoma following intravenous administration of saline, free DOX (5 mg/kg), CatB-NPs (L) (DOX equivalent to 5 mg/kg), or CatB-NPs (H) (DOX equivalent to 10 mg/kg) every 3 d for 12 d; (B) Images and weight measurements of excised tumors at the study endpoint; (C, D) Histological evaluation of tumor tissues by H&E staining for structural alterations and TUNEL staining for apoptosis quantification; (E-G) Quantitative analysis of ICD-associated DAMPs in tumor tissues, including surface-exposed CRT, extracellular ATP release, and HMGB1 secretion; (H) Flow cytometric analysis of tumor-infiltrating mature DCs ($CD11c^+CD40^+CD86^+$); (I) Flow cytometric quantification of $CD3^+CD8^+CD107a^+$ T cells to evaluate cytotoxic T cell activity; (J) IHC staining of tumor sections to visualize and quantify intratumoral $CD25^+$ regulatory T cells ($CD45^+CD3^+CD4^+CD25^+$).

monitoring time in all treatment groups, minimizing necrosis- and inflammation-associated confounding effects on immune analysis [37]. CatB-NPs (H) and free DOX were intravenously injected every 3 d, and aPD-L1 was intraperitoneally administered at the same interval until Day 12, with tumor growth monitored until Day 30.

During the 30-d monitoring period, tumor progression reached the ethical endpoint (>2000 mm^3) at different time points in each group. The saline-treated group rapidly progressed to 2490.49 ± 371.06 mm^3 by 12 d, while the aPD-L1 group reached 2270.45 ± 446.65 mm^3 by 16 d In the free DOX+aPD-L1 group, tumor growth was delayed but still enlarged to 1934.10 ± 628.84 mm^3 by 28 d In contrast, the CatB-NPs (H)+aPD-L1 group maintained durable tumor suppression until the end of the 30-d period, with a mean residual volume of 28.37 ± 31.73 mm^3 and CR achieved in 3 of 5 mice (Fig. 4A). Representative tumor images and weight measurements from each treatment group ($n = 3$ per group) are provided (Fig. S13), which illustrate the overall tumor regression profiles and highlighted the CR observed in the CatB-NPs (H)+aPD-L1 group.

Importantly, at the treatment endpoint of 12 d, free DOX+aPD-L1 group showed a mean tumor volume of 433.34 ± 81.56 mm^3, corresponding to a ~43% reduction compared with free DOX monotherapy (767.35 ± 282.47 mm^3), thereby confirming the short-term synergistic effect of ICD induction and ICB blockade. However, this effect was not durable, as most mice lost more than 15%–20% of their weight, reflecting severe systemic toxicity and had already reached the humane endpoint by 16–18 d In the remaining animals, tumors regrew rapidly, exceeding 2000 mm^3 by 29 d, and the final mean volume reached 1934 ± 628.83 mm^3. This pattern of early toxicity or eventual recurrence is consistent with the aggressive, immune-evasive, and drug-resistant properties of melanoma. These results highlight the inherent limitations of conventional free DOX-based chemotherapy, including acute systemic toxicity, indiscriminate immune cell damage, limited treatment duration, and inability to overcome immune evasion in aggressive melanoma. In contrast, CatB-NPs (H)+aPD-L1 group maintained CR without relapse throughout the 30-d observation period and exhibited only a 7.1% body weight loss, representing a marked improvement compared with the 17.99% reduction observed in free DOX+aPD-L1 group (Fig. S14). Notably, H&E and TUNEL staining showed a significant increase in structural damage and cell death in CatB-NPs (H)+aPD-L1 group, compared with all other groups (Fig. 4B), which was further demonstrated by quantitative TUNEL analysis (Fig. S15). From these results, free DOX+aPD-L1 group provided only short-term suppression but was undermined by relapse and toxicity. In contrast, CatB-NPs

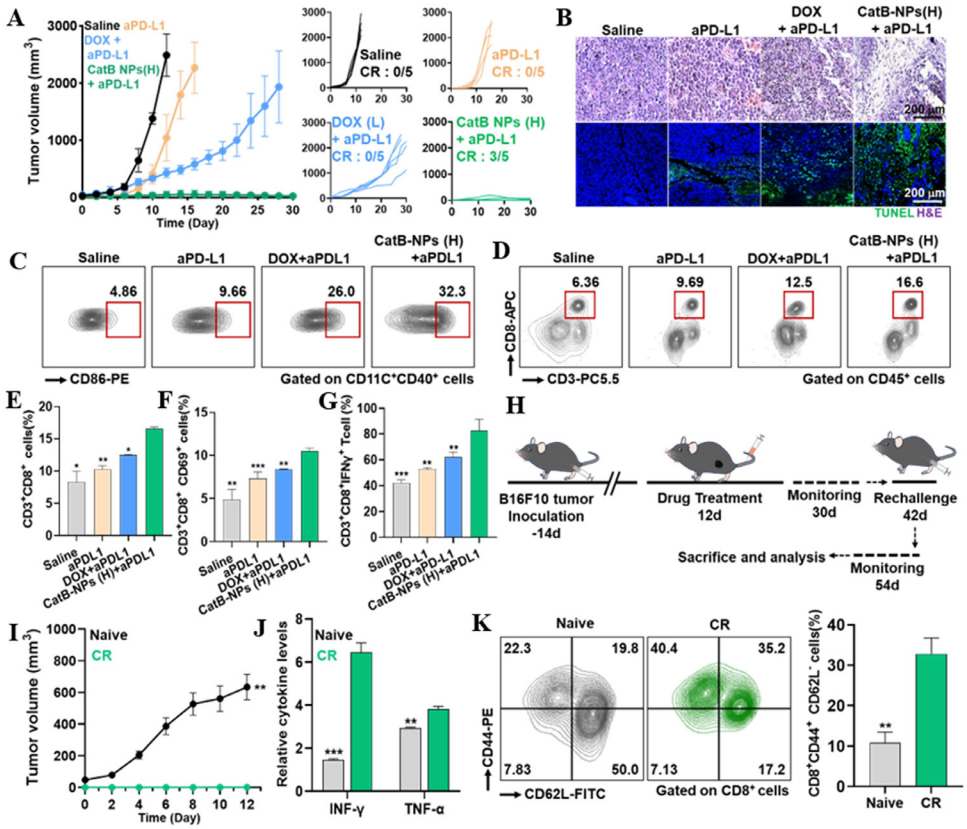


Fig. 4 – Synergistic tumor inhibition and durable immune memory in B16F10 melanoma-bearing mice induced by CatB-NPs and aPD-L1 combination therapy. (A) Tumor growth curves in C57BL/6 mice ($n = 5$) bearing B16F10 melanoma following intravenous administration of saline, aPD-L1, DOX (5 mg/kg)+aPD-L1, or CatB-NPs (H) (DOX equivalent to 10 mg/kg)+aPD-L1 for 12 d, with tumor growth monitored until 30 d without further treatment; (B) Histological evaluation of structural disruption and apoptosis by H&E and TUNEL staining; (C-G) Immune profiling of tumor tissues on Day 12, including quantification of mature DCs ($CD11c^+CD40^+CD86^+$); cytotoxic T cells ($CD45^+CD3^+CD8^+$); activated T cells ($CD3^+CD8^+CD69^+$); and effector T cells ($CD3^+CD8^+IFN\text{-}\gamma^+$); (H, I) Tumor rechallenge in naïve and complete remission (CR) mice ($n = 3$) by subcutaneous inoculation of B16F10 cells at Day 42 post-treatment, with tumor growth monitored for 12 d; (J) Plasma cytokine levels (IFN-γ, TNF-α) at Day 12 after rechallenge compared between CR and naïve mice. (K) Flow cytometric analysis of splenic memory T cells ($CD8^+CD44^+CD62L^{\wedge}low$) in CR and naïve mice.

(H) achieved durable, relapse-free regression with minimal toxicity, underscoring its clear advantage over conventional DOX-based chemoimmunotherapy.

Next, to investigate the immune mechanisms of CatB-NPs (H)+aPD-L1 group, a separate experimental group was sacrificed on Day 12 for FACS analysis. Tumor tissues from CatB-NPs (H)+aPD-L1 group exhibited markedly higher proportions of mature DCs ($CD11c^+CD40^+CD86^+$), showing 6.3-fold, 3.1-fold, and 1.3-fold increases compared with saline, aPD-L1, and DOX+aPD-L1 groups, respectively (Fig. 4C and S16), indicating enhanced antigen presentation. This was accompanied by a marked rise in intratumoral $CD8^+$ T cells ($CD45^+CD3^+CD8^+$), which increased by ~2.0-fold compared to saline group and 1.6-fold compared to aPD-L1 group, and 1.3-fold compared to DOX+aPDL1 group confirming enhanced cytotoxic T cell infiltration. Among these, $CD69^+CD8^+$ T cells were elevated by 2.13-fold relative to saline group and 1.43-fold relative to aPD-L1 group, 1.24-fold relative to DOX+aPDL1 group highlighting enhanced early activation (Fig. 4D-4F). Subsequently, the proportion of IFN-γ^+ CD8 T cells was significantly increased by 2.19-fold compared to saline group and 1.70-fold compared to aPD-L1 group, 1.42-fold compared to DOX+aPDL1 group confirming the functional activation of cytotoxic T cells and their direct involvement in tumor clearance (Fig. 4G). To assess whether the CR achieved in CatB-NPs (H)+aPD-L1 group was accompanied by long-term immune memory, a tumor rechallenge experiment was performed (Fig. 4H). Naïve and CR mice ($n = 3$) were subcutaneously inoculated with B16F10 cells (1×10^5 cells/mouse). While naïve mice exhibited rapid tumor growth (634.80 ± 81.09 mm^3 at Day 12), CR mice showed no detectable tumor formation, indicating the establishment of durable, tumor-specific immune memory (Fig. 4I). On Day 12 post-rechallenge, CR mice displayed significantly elevated frequencies of IFN-γ and TNF-α, ~2.3-fold higher than in naïve controls, confirming the functional recall capacity of memory T cells (Fig. 4J). In parallel, the proportion of splenic effector/memory T cells (Tem; $CD3^+CD8^+CD44^+CD62L^{low}$)

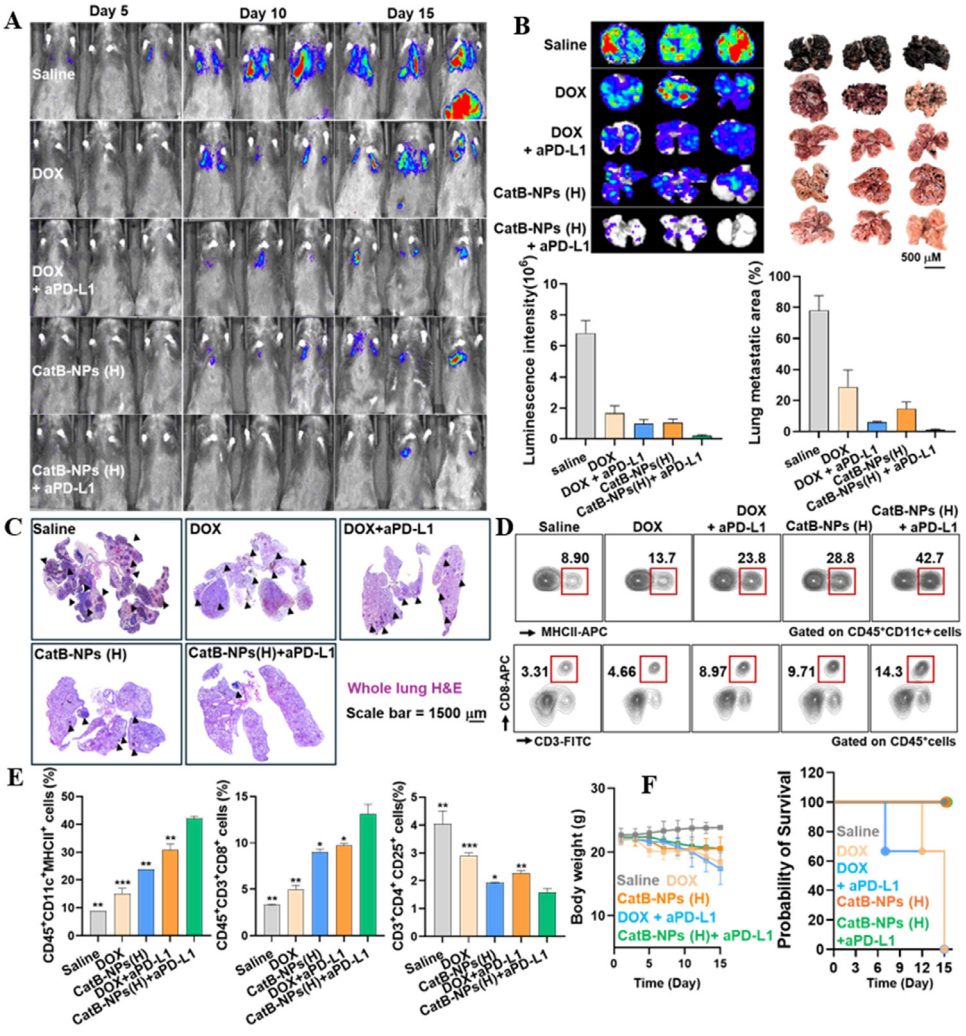


Fig. 5 – Therapeutic efficacy of CatB-NPs combined with aPD-L1 in a pulmonary metastatic B16F10 melanoma model. (A) Bioluminescence imaging of lung metastases on Day 5, 10 and 15 in C57BL/6 mice ($n = 3$) treated with saline, free DOX (5 mg/kg), CatB-NPs(H) (DOX equivalent to 10 mg/kg), DOX (5 mg/kg)+aPD-L1 (10 mg/kg), or CatB-NPs(H)+aPD-L1 (10 mg/kg); (B) *Ex vivo* luminescence and optical imaging of excised lungs with quantitative analysis of metastatic burden; (C) H&E staining of lung tissues with metastatic lesions indicated by arrows; (D,E) Flow cytometry analysis of tumor-infiltrating immune cells, including DCs ($CD45^+CD11c^+MHC\text{-}II^+$), cytotoxic T cells ($CD45^+CD3^+CD8^+$), and regulatory T cells ($CD45^+CD3^+CD4^+CD25^+$). (F) Body weight and survival monitoring (euthanasia at 15%–20% weight loss).

was also 3.02-fold higher in CR mice compared to naïve, further supporting the establishment of long-term immune protection (Fig. 4K). Collectively, these results demonstrate that high-dose CatB-NPs overcome intrinsic drug resistance and systemic toxicity in melanoma, while inducing strong ICD and enhancing ICB efficacy.

3.5. *Therapeutic efficacy of CatB-NPs combined with APD-L1 in a pulmonary metastatic B16F10 melanoma model*

Finally, we evaluated the therapeutic efficacy of high-dose CatB-NPs in a pulmonary metastatic tumor model. To establish pulmonary metastases, luciferase-expressing B16F10 melanoma cells (4×10^5) were intravenously injected into C57BL/6 mice. Mice were randomly assigned into five groups ($n = 3$) and intravenously administered every 3 d with: (i) saline, (ii) free DOX (5 mg/kg), (iii) DOX + aPD-L1 (10 mg/kg), (iv) high-does CatB-NPs (H; 10 mg/kg DOX equiv.), or (v) high-does CatB-NPs (H) + aPD-L1. Tumor growth was monitored on Day 5, 10 and 15 by non-invasive bioluminescence imaging (Fig. 5A and S17). Mice in the saline group exhibited strong luminescence signals from 10 d, indicative of rapid metastatic progression. Free DOX and high-does CatB-NPs(H) monotherapy group delayed tumor growth until Day 10 but failed to maintain suppression by 15 d It was reported that anti-PD-L1 monotherapy in the same B16F10 metastatic model did not show sufficient therapeutic efficacy, which is comparable to the PBS control groups [38]. Furthermore, anti-PD-L1 monotherapy did not induce T cell-mediated immune responses. Notably, on Day

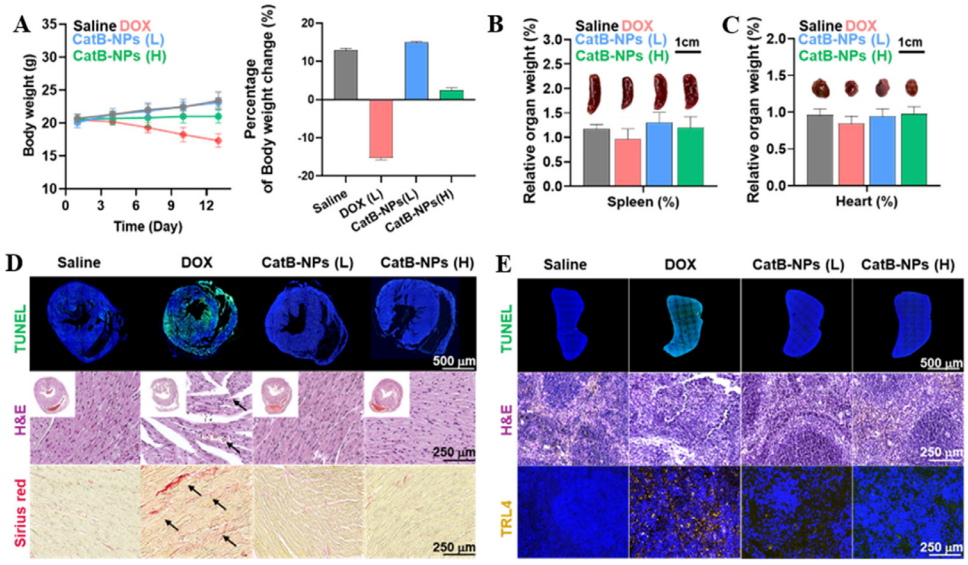


Fig. 6 – *In vivo* safety evaluation of CatB-NPs. (A) Body weight monitoring in C57BL/6 mice ($n = 5$) treated every 3 d for 12 d with saline, free DOX (5 mg/kg), or CatB-NPs (L/H) (DOX equivalent to 5 or 10 mg/kg); (B, C) Images of excised heart and spleen with corresponding weight quantification at Day 14; (D) Histological staining of heart tissues on Day 12, with whole-section TUNEL and H&E to assess apoptosis, and Sirius Red to evaluate fibrosis(red); (E) Histological staining of spleen tissues on Day 14, including whole-section TUNEL and H&E for apoptosis and TLR4 (yellow) immunostaining for inflammation.

15, the high-dose CatB-NPs (H) group exhibited a 2.6-fold lower luminescence intensity compared with the free DOX group, indicating improved tumor suppression. Moreover, both combination therapies achieved stronger tumor suppression than their respective monotherapies. Importantly, CatB-NPs (H) + aPD-L1 was markedly superior, reducing tumor luminescence by approximately 48-fold compared with the DOX + aPD-L1 group. *Ex vivo* lung tissue luminescence analysis further supported these findings, demonstrating superior antitumor efficacy of the combination groups compared with their respective monotherapies. In particular, the high-dose CatB-NPs (H) + aPD-L1 group exhibited the most distinct effect, reducing luminescence by 34.1-fold relative to the saline group, 8.3-fold relative to free DOX, 4.9-fold relative to DOX + aPD-L1, and 5.2-fold relative to high-does CatB-NPs (H). Notably, in this group, one mouse displayed a complete absence of detectable luminescence signal. Consistent with these results, optical images revealed extensive metastatic nodules in the saline group, whereas the high-dose CatB-NPs (H) + aPD-L1 group exhibited the fewest and smallest lesions. Quantification of metastatic area confirmed this trend, indicating suppression of lung metastases (Fig. 5B). H&E staining of lung tissues revealed a clear reduction in metastatic lesions in high-does CatB-NPs(H)+aPD-L1 group, confirming the pronounced inhibitory effect on tumor progression (black arrows; Fig. 5C). Flow cytometry analysis demonstrated that combination treatment with high-dose CatB-NPs (H) + aPD-L1 markedly enhanced both ICD- and ICB-mediated responses compared with other groups. The proportion of mature DCs ($CD45^+CD11c^+MHC\text{-}II^+$) increased 4.7-fold relative to saline, whereas DOX, high-does CatB-NPs (H), and DOX + aPD-L1 groups showed 1.7-, 2.7- and 3.5-fold increases, respectively. Cytotoxic T cells ($CD45^+CD3^+CD8^+$) were also expanded, reaching 3.9-fold in the high-does CatB-NPs (H) + aPD-L1 group compared with saline, in contrast to 1.5-, 2.7-, and 2.9-fold increases in DOX, high-does CatB-NPs (H), and DOX + aPD-L1 groups. Regulatory T cells ($CD45^+CD3^+CD4^+CD25^+$) were significantly decreased, with high-dose CatB-NPs (H) + aPD-L1 producing the greatest reduction (0.39-fold of saline). The relative values were 0.72-fold for DOX, 0.48-fold for CatB-NPs (H), and 0.56-fold for DOX + aPD-L1 (Fig. 5D, 5E and S18).

These immune alterations in high-does CatB-NPs (H)+aPD-L1-treated metastatic tumor tissues were driven by cancer cell-specific ICD induction and high-dose intratumoral drug accumulation, which preserved normal and immune cells from chemotherapy-induced toxicity and amplified the overall antitumor response. Body weight monitoring revealed the marked systemic toxicity of DOX-based therapy. Free DOX treatment resulted in ~17% body weight loss despite limited therapeutic benefit, and the DOX + aPD-L1 combination induced an even greater reduction of ~21%, approaching the humane endpoint threshold and highlighting the dose-limiting toxicity of conventional DOX regimens. In contrast, high-dose CatB-NPs (H) caused only ~7% weight loss, and the high-dose CatB-NPs (H) + aPD-L1 group maintained survival with a modest ~8% reduction, demonstrating markedly improved tolerability. These results indicate that CatB-NPs allow high-dose DOX delivery with tumor selectivity, thereby preserving strong antitumor efficacy while substantially reducing systemic toxicity (Fig. 5F). In this aggressive lung metastasis model, high-dose CatB-NPs enabled sustained intratumoral drug accumulation that was not achievable with conventional DOX regimens, driving cancer cell-specific apoptosis and potent ICD induction. When combined with

aPD-L1, this high-dose strategy produced robust and durable antitumor immunity while minimizing systemic toxicity and preserving immune cell function.

3.6. *In vivo safety evaluation of high-dose CatB-NPs therapy*

To evaluate the *in vivo* safety of CatB-NPs, C57BL/6 mice ($n = 5$) were intravenously administered with saline, free DOX (5 mg/kg), low-does CatB-NPs (L) (5 mg/kg DOX equiv.), or high-does CatB-NPs (H) (10 mg/kg DOX equiv.) every 3 d for 12 d, following the same protocol used for therapeutic efficacy evaluation, and monitored for 14 d with body weight measured on Day 1, 4, 7, 10 and 13 (Fig. 6A). At the end of the monitoring period, body weight increased in the saline (+13.0%) and low-does CatB-NPs (L) (+14.9%) groups and high-does CatB-NPs (H) group (+2.4%) maintained the weight for 12 d However, the free DOX group showed a distinct weight loss (−15.3%), indicating systemic toxicity. Organ weight measurements showed no weight loss in low-does CatB-NPs (L) or high-does CatB-NPs (H) groups compared with saline, while free DOX group exhibited significant decreases in heart (−12.5%) and spleen (−23.1%) weights, suggesting non-specific organ toxicity (Fig. 6B and 6C). In TUNEL, H&E, and Sirius Red-stained heart sections, the saline and CatB-NPs (L)/(H) groups showed no detectable apoptosis, fibrosis, or inflammation, whereas free DOX group displayed strong TUNEL signals, structural disruption, and marked fibrosis (black arrows) (Fig. 6D). Similarly, in the case of spleen stained with TUNEL, H&E, and TLR4, CatB-NPs (L)/(H) groups maintained structural integrity, while the free DOX group showed extensive apoptosis, inflammation, and tissue disorganization (Fig. 6E). Notably, the preservation of splenic structure suggests that CatB-NPs may protect immune cell function and thereby contribute to the enhancement of antitumor immunity. Additionally, H&E staining of the liver, lung, and kidney revealed no apparent toxicity in the CatB-NPs (L)/(H) groups (Fig. S19). Furthermore, hematological analyses supported that CatB-NPs (L)/(H) groups did not cause organ-specific toxicity (Fig. S20). These findings highlight that high-dose CatB-NPs (H) achieve robust tumor-selective ICD induction while avoiding off-target toxicity in major organs, thereby overcoming the dose-limiting toxicity of conventional DOX and enabling sustained, safe chemo-immunotherapy.

4. Conclusion

In this study, we propose a high-dose chemo-immunotherapy strategy for immune-cold melanoma based on tumor-activatable prodrug nanoparticles (CatB-NPs), which are selectively cleaved by cathepsin B. The CatB-NPs spontaneously released free DOX exclusively within cathepsin B-overexpressing TME, thereby inducing cancer cell-specific apoptosis and ICD while minimizing damage to normal cells and immune cells. This tumor-specific ICD promoted DC maturation and T cell activation, converting the immunosuppressive melanoma microenvironment into an immune-responsive state. Importantly, high-dose CatB-NPs treatment showed tumor-specific ICD without systemic toxicity in melanoma tumor models, resulting in enhanced antitumor efficacy. Notably, when combined with aPD-L1, CatB-NPs achieved complete tumor regression, thereby overcoming the low response rate of ICB monotherapy. In contrast, free DOX caused non-specific toxicity to normal tissues, such as heart and spleen, whereas CatB-NPs maintained splenic and cardiac function as well as immune cell viability-an essential condition for achieving complete tumor clearance in combination with aPD-L1. Furthermore, CatB-NPs promoted long-term immune memory, preventing recurrence in tumor rechallenge models. In the pulmonary metastasis model, CatB-NPs effectively suppressed metastatic tumor progression and established durable immune protection against reintroduced tumors. Overall, high-dose CatB-NPs showed excellent tumor-specific ICD induction and an effective ICB response in inoculated and metastatic melanoma models with minimal systemic toxicity.

Conflicts of interest

The authors declare that there is no conflicts of interest.

CRediT authorship contribution statement

Yoojeong Oh: Validation, Investigation, Formal analysis, Data curation. **Jinseong Kim:** Writing – original draft, Visualization, Methodology, Conceptualization. **Nayeon Shim:** Formal analysis. **Hyeonji Yoo:** Data curation. **Hoyeon Lee:** Formal analysis. **Yumin Jeong:** Formal analysis. **Jagyeong Goo:** Formal analysis. **Jeongyeon Lee:** Formal analysis. **Mihee Jo:** Methodology. **Hanhee Cho:** Visualization, Methodology, Conceptualization. **Kwangmeyung Kim:** Writing – review & editing, Supervision, Resources, Project administration, Funding acquisition, Conceptualization.

Acknowledgements

This work was supported by the National Research Foundation of Korea (NRF) grant funded by the Korea government (MSIT) (RS-2024-00351185, RS-2025-02219039), by the Korea Health Industry Development Institute (KHIDI) grant funded by the Korea government (MOHW) (RS-2023-KH135133), and by Korea Drug Development Fund (KDDF) funded by Ministry of Science and ICT, Ministry of Trade, Industry, and Energy, and Ministry of Health and Welfare (RS-2025-02223093).

Supplementary materials

Supplementary material associated with this article can be found, in the online version, at doi:10.1016/j.ajps.2026.101123. The figures and tables with “S” before the serial number are included in the Supplementary data.

References

[1] Zhou L, Zhong Y, Han L, Xie Y, Wan M. Global, regional, and national trends in the burden of melanoma and non-melanoma skin cancer: insights from the global burden of disease study 1990–2021. Sci Rep 2025;15:5996.

[2] Fateeva A, Eddy K, Chen S. Current state of melanoma therapy and next steps: battling therapeutic resistance. Cancers (Basel) 2024;16:1571.

[3] Patel M, Eckburg A, Gantiwala S, Hart Z, Dein J, Lam K, et al. Resistance to molecularly targeted therapies in melanoma. Cancers (Basel) 2021;13:230.

[4] Lipson EJ, Drake CG. Ipilimumab: an anti-CTLA-4 antibody for metastatic melanoma. Clin Cancer Res 2011;17:6958–62.

[5] Wolchok JD, Chiarion-Sileni V, Gonzalez R, Grob JJ, Rutkowski P, Lao CD, et al. Long-term outcomes with nivolumab plus ipilimumab or nivolumab alone *versus* ipilimumab in patients with advanced melanoma. J Clin Oncol 2022;40:127–37.

[6] Liu YT, Sun ZJ. Turning cold tumors into hot tumors by improving T-cell infiltration. Theranostics 2021;11:5365–86.

[7] Ghiringhelli F, Rébé C. Using immunogenic cell death to improve anticancer efficacy of immune checkpoint inhibitors: from basic science to clinical application. Immunol Rev 2024;321:335–49.

[8] Bezu L, Gomes-da-Silva LC, Dewitte H, Breckpot K, Fucikova J, Spisek R, et al. Combinatorial strategies for the induction of immunogenic cell death. Front Immunol 2015;6:187.

[9] Pollack SM, Redman MW, Baker KK, Wagner MJ, Schroeder BA, Loggers ET, et al. Assessment of doxorubicin and pembrolizumab in patients with advanced anthracycline-naive sarcoma: a phase 1/2 nonrandomized clinical trial. JAMA Oncol 2020;6:1778–82.

[10] Wessely A, Steeb T, Berking C, Heppt MV. How neural crest transcription factors contribute to melanoma heterogeneity, cellular plasticity, and treatment resistance. Int J Mol Sci 2021;22:5761.

[11] Baronzio G, Parmar G, Baronzio M. Overview of methods for overcoming hindrance to drug delivery to tumors, with special attention to tumor interstitial fluid. Front Oncol 2015;5:165.

[12] Porrata LF, Adjei AA. The pharmacologic basis of high dose chemotherapy with haematopoietic stem cell support for solid tumours. Br J Cancer 2001;85:484–9.

[13] Pedrazzoli P, Ledermann JA, Lotz JP, Leyvraz S, Aglietta M, Rosti G, et al. High dose chemotherapy with autologous hematopoietic stem cell support for solid tumors other than breast cancer in adults. Ann Oncol 2006;17:1479–88.

[14] Amiri M, Molavi O, Sabetkam S, Jafari S, Montazersaheb S. Stimulators of immunogenic cell death for cancer therapy: focusing on natural compounds. Cancer Cell Int 2023;23:200.

[15] Liu Y, Yan W, Tohme S, Chen M, Fu Y, Tian D, et al. Hypoxia induced HMGB1 and mitochondrial DNA interactions mediate tumor growth in hepatocellular carcinoma through Toll-like receptor 9. J Hepatol 2015;63:114–21.

[16] Hoek J, Bloemendal KM, van der Velden LA, van Diessen JN, van Werkhoven E, Klop WM, et al. Nephrotoxicity as a dose-limiting factor in a high-dose cisplatin-based chemoradiotherapy regimen for head and neck carcinomas. Cancers (Basel) 2016;8:21.

[17] Smith LA, Cornelius VR, Plummer CJ, Levitt G, Verrill M, Canney P, et al. Cardiotoxicity of anthracycline agents for the treatment of cancer: systematic review and meta-analysis of randomised controlled trials. BMC Cancer 2010;10:337.

[18] Teixeira AAS, Biondo LA, Silveira LS, Lima EA, Batatinha HA, Diniz TA, et al. Doxorubicin modulated clock genes and cytokines in macrophages extracted from tumor-bearing mice. Cancer Biol Ther 2020;21:344–53.

[19] Catanzaro E, Beltrán-Visiedo M, Galluzzi L, Krysko DV. Immunogenicity of cell death and cancer immunotherapy with immune checkpoint inhibitors. Cell Mol Immunol 2025;22:24–39.

[20] Yang L, Xu J, Xie Z, Song F, Wang X, Tang R. Carrier-free prodrug nanoparticles based on dasatinib and cisplatin for efficient antitumor *in vivo*. Asian J Pharm Sci 2021;16:762–71.

[21] Wang Y, Ye H, von Arx D, Li Y, Wang Y, Mesot A, et al. Magnetic continuum soft robot-driven precise delivery of prodrug nanoassemblies for gastric cancer chemo-immunotherapy. Asian J Pharm Sci 2025;20:101103.

[22] Kim J, Shim MK, Yang S, Moon Y, Song S, Choi J, et al. Combination of cancer-specific prodrug nanoparticle with Bcl-2 inhibitor to overcome acquired drug resistance. J Control Release 2021;330:920–32.

[23] Shim MK, Yang S, Park J, Yoon JS, Kim J, Moon Y, et al. Preclinical development of carrier-free prodrug nanoparticles for enhanced antitumor therapeutic potential with less toxicity. J Nanobiotechnol 2022;20:436.

[24] Shim N, Jeon SI, Yang S, Park JY, Jo M, Kim J, et al. Comparative study of cathepsin B-cleavable linkers for the optimal design of cathepsin B-specific doxorubicin prodrug nanoparticles for targeted cancer therapy. Biomaterials 2022;289:121806.

[25] Kim J, Shim MK, Cho YJ, Jeon S, Moon Y, Choi J, et al. The safe and effective intraperitoneal chemotherapy with cathepsin B-specific doxorubicin prodrug nanoparticles in ovarian cancer with peritoneal carcinomatosis. Biomaterials 2021;279:121189.

[26] Yang S, Shim MK, Kim WJ, Choi J, Nam GH, Kim J, et al. Cancer-activated doxorubicin prodrug nanoparticles induce preferential immune response with minimal doxorubicin-related toxicity. Biomaterials 2021;272:120791.

[27] Shim MK, Park J, Yoon HY, Lee S, Um W, Kim JH, et al. Carrier-free nanoparticles of cathepsin B-cleavable peptide-conjugated doxorubicin prodrug for cancer targeting therapy. J Control Release 2019;294:376–89.

[28] Li Y, Li L, Jin Q, Liu T, Sun J, Wang Y, et al. Impact of the amount of PEG on prodrug nanoassemblies for efficient cancer therapy. Asian J Pharm Sci 2022;17:241–52.

[29] Huang Y, Lin Y, Li B, Zhang F, Zhan C, Xie X, et al. Combination therapy to overcome ferroptosis resistance by biomimetic self-assembly nano-prodrug. Asian J Pharm Sci 2023;18:100844.

[30] Song L, Qiu Q, Ju F, Zheng C. Mechanisms of doxorubicin-induced cardiac inflammation and fibrosis; therapeutic targets and approaches. Arch Biochem Biophys 2024;761:110140.

[31] Xu S, Liu C, Zang S, Li J, Wang Y, Ren K, et al. Multifunctional self-delivery micelles targeting the invasion-metastasis cascade for enhanced chemotherapy against melanoma and the lung metastasis. Asian J Pharm Sci 2021;16:794–805.

[32] Jadapalli JK, Wright GW, Kain V, Sherwani MA, Sonkar R, Yusuf N, et al. Doxorubicin triggers splenic contraction and irreversible dysregulation of COX and LOX that alters the inflammation-resolution program in the myocardium. Am J Physiol Heart Circ Physiol 2018;315:H1091–100.

[33] Kim Y, Kim J, Jeong JH, Kim I, Shim N, Yoo H, et al. Cancer-specific and pro-apoptotic PEGylated liposomes containing SMAC-mimetic doxorubicin prodrug for safe high-dose delivery in pancreatic cancer. Adv Healthc Mater 2024;13:e02018.

[34] Cui Y, Miao Y, Cao L, Guo L, Cui Y, Yan C, et al. Activation of melanocortin-1 receptor signaling in melanoma cells impairs T cell infiltration to dampen antitumor immunity. Nat Commun 2023;14:5740.
[35] Nitiss JL. Targeting DNA topoisomerase II in cancer chemotherapy. Nat Rev Cancer 2009;9:338–50.
[36] Kim J, Shim MK, Moon Y, Kim J, Cho H, Yun WS, et al. Cancer cell-specific and pro-apoptotic SMAC peptide-doxorubicin conjugated prodrug encapsulated aposomes for synergistic cancer immunotherapy. J Nanobiotechnol 2024;22:109.
[37] Yee PP, Li W. Tumor necrosis: a synergistic consequence of metabolic stress and inflammation. Bioessays 2021;43:e2100029.
[38] Li H, Wang Z, Chen Z, Ci T, Chen G, Wen D, et al. Disrupting tumour vasculature and recruitment of aPDL1-loaded platelets control tumour metastasis. Nat Commun 2021;12:2773.